

# Numerical investigation of the effect of macro control measures on epidemics transport via a coupled PDE crowd flow - epidemics spreading dynamics model

A.I. Delis

School of Production Engineering & Management,  
Technical University of Crete,  
University Campus, Chania, Greece, 73100  
adelis@tuc.gr

N. Bekiaris-Liberis

School of Production Engineering & Management,  
Technical University of Crete,  
University Campus, Chania, Greece, 73100  
bekiaris-liberis@ece.tuc.gr

November 26, 2024

## Abstract

This work aims to provide an approach to the macroscopic modeling and simulation of pedestrian flow, coupled with contagion spreading, towards numerical investigation of the effect of certain, macro-control measures on epidemics transport dynamics. To model the dynamics of the pedestrians, a second-order macroscopic model, coupled with an Eikonal equation, is used. This model is coupled with a macroscopic Susceptible-Exposed-Infected-Susceptible-Vaccinated (SEISV) contagion model, where the force-of-infection  $\beta$  coefficient is modeled via a drift-diffusion equation, which is affected by the air-flow dynamics due to the ventilation. The air-flow dynamics are obtained assuming a potential flow that can imitate the existence of ventilation in the computational domain. Numerical approximations are considered for the coupled model along with numerical tests and results. In particular, we investigate the effect of employment of different, epidemics transport control measures, which may be implemented through real-time manipulation of i) ventilation rate and direction, ii) maximum speed of pedestrians, and iii) average distances between pedestrians, and through iv) incorporation in the crowd of masked or vaccinated individuals. Such simulations of disease spreading in a moving crowd can

potentially provide valuable information about the risks of infection in relevant situations and support the design of systematic intervention/control measures.

Keywords: Crowd Flow, Epidemics Spreading, Macroscopic Models, Numerical Solution

## 1 Introduction

The ramifications of epidemics spreading in economy [3] and physical/mental health [8], highlighted the need of accurate prediction of epidemics spreading. One way towards this is through modeling the dynamics of epidemics spreading. Due to the complexity of detailed description of epidemics spreading when accounting for individual-to-individual interactions, see, for example, [36], macroscopic models may be utilized to describe epidemics spreading dynamics, particularly in cases of large crowds/spaces, see, for example, [34]. Even though such models capture epidemics spreading dynamics on a macroscopic scale, they may not capture the transporting behavior of epidemics, which is, in fact, the main, macroscopic phenomenon in epidemics spreading dynamics, emerging from people transport. Furthermore, there are at least four potential macroscopic ways of control of epidemics spreading in closed spaces, namely via manipulation of the air-flow rate and direction, see, e.g., [14], or via real-time manipulation of the maximum speed of and average distances between pedestrians (through recommendations or other means), see, for example, [16, 35, 12, 33], or via incorporating in the crowd masked/vaccinated individuals. For these two reasons, in the present work, we perform numerical tests to study the epidemics transport dynamics, under the effect of various ventilation air-flow rates/directions, for various values of the maximum pedestrians' speed and of their average distances, and in the presence of masked/vaccinated individuals, utilizing a Partial Differential Equation (PDE) model that accounts for crowd flow and epidemics spreading dynamics, as well as for the effect of ventilation.

Macroscopic modeling of coupled crowd motion and epidemic spreading dynamics is relatively unexplored. Here we provide such a model that may be useful in situations of crowds occupying confined spaces where a disease may easily spread such as, e.g., measles, influenza, or COVID-19. In particular, we utilize a PDE model consisting of three components; a component that describes crowd flow dynamics in two-dimensional (2D) spaces, a component that describes epidemics spreading, essentially, being a macroscopic version of a SEISV-type model, and a component that describes the effect of aerosol dynamics to spreading, in particular, describing the effect of ventilation induced air-flow. The model we present here can be viewed as a modified version of the model considered in [27], in that we use a less complex crowd flow model (modified from [16] and [22]) and use potential theory to compute the ventilation induced air-flow field, besides also incorporating transport dynamics for masked/vaccinated individuals. Papers [26], [18], and [1] also present relevant

PDE models<sup>1</sup>, consisting of a crowd flow dynamics component and an epidemics spreading component with a different type of infection coefficient. Our work can be also viewed as relevant to papers that consider macroscopic models of people mobility (via describing the respective traffic flow dynamics) and epidemics spreading dynamics, such as, e.g., [11, 28, 4, 29, 6, 10, 23]. Although these works are relevant, they describe the coupled people flow - epidemics spreading process on a higher, macroscopic level (e.g., on the level of a country or a city), not considering the crowd movements in closed spaces. Therefore, here we employ an integrated model that considers the interactions between pedestrian movements and disease transmission dynamics in closed spaces, enabling the assessment of how crowd dynamics influence disease spreading in relevant scenarios.

In the present paper, we perform numerical tests employing the proposed PDE model. In particular, we employ a second-order, accurate finite-volume-based numerical scheme to simultaneously solve on a 2D domain the three components of the model, namely, the crowd flow, epidemics spreading, and aerosol dynamics models; while employing a finite-difference scheme for numerically solving a 2D Laplace equation to obtain a simplified velocity field (based on potential theory), corresponding to the operation of the ventilation system. Implementing these numerical schemes, we categorize the tests performed in three different types as follows. In the first, we consider people moving towards a single exit, together with accounting for variable ventilation rates, different air-flow directions, different maximum speed and pressure coefficients, as well as accounting for the presence of masked/vaccinated individuals. In the second, we perform similar tests, but in comparison with the first type of tests, we consider two exits. In the third, we account for a larger space and a larger number of total individuals moving towards an exit.

Based on the results from the tests performed we compare the various potential macro control measures with respect to the resulting total number of exposed individuals, which is considered as an index of spreading degree. In general, our findings indicate that the total number of exposed individuals decreases with an increase in the ventilation rate, or when people move against the direction of air-flow, or when the maximum speed of individuals increases, or when the pressure coefficient increases (implying larger average distances between individuals), or when masked/vaccinated individuals are included in the crowd. However, the effect of increased pressure coefficient is less significant when the flow capacity on the exit is large; while when the flow capacity at the exit is low, further increasing the maximum speed may not be beneficial for spreading. The exact quantification of the total number of individuals depends on the actual magnitudes of ventilation rate, maximum speed, and pressure coefficients, as well as the number of masked/vaccinated individuals. Essentially, our results illustrate the possibility to utilize the density (and speed) profile in time/space in real time (i.e., to not only employing an average, total number of people), to manipulate ventilation air-flow field in closed spaces towards bal-

---

<sup>1</sup>Although here we review only PDE macroscopic models, there exist microscopic models, which describe coupled pedestrians-epidemics transport dynamics, accounting for movements of individuals and individual-to-individual interactions, see, e.g., [11].

ancing epidemics spreading suppression and energy, as well as to manipulate in a systematic manner, the average distances between individuals and their maximum speed (via, e.g., recommendations from speakers), towards epidemics spreading suppression.

The paper is organized as follows. We start in Section 2 presenting the coupled crowd flow-epidemics spreading dynamics model. In Section 3 we present the numerical schemes employed for solving the complete model. In Section 4 we present and interpret the simulation results obtained from the numerical implementation of the model. We provide concluding remarks in Section 5.

## 2 Coupled Modeling Equations

### 2.1 Crowd Flow Modeling

The model presented here is classified as a nonlinear, hyperbolic PDE system (with source terms present). Second-order models in 2D use three-coupled PDEs to describe crowd flow; the mass conservation and two equations that resemble the momentum equations in fluid flow with a modification to the pressure term to mimic crowd motion. In essence, we consider pedestrians as a “thinking fluid”. The model considered here is known for its isotropic nature, which is realistic assuming pedestrian motion is influenced from all directions. This model stems from the well-known Payne-Whitam (PW) traffic flow model, [21, 24], adapted to crowd dynamics [16, 22]. We present the model in conservation law form, which eases the application of proper numerical methods (e.g., finite volume ones). In general, we consider a 2D connected domain  $\Omega \subset \mathbb{R}^2$  corresponding to some walking facility, possibly equipped with some entrances or exits. In this work, we do not consider the case of having some entrances, thus the boundary of the domain  $\partial\Omega = \Gamma_0 \cup \Gamma_w$ , where outflow boundaries are denoted by  $\Gamma_0$  and the walls by  $\Gamma_w$ .

By denoting as  $\mathbf{x} = (x, y) \in \Omega$  the spatial variables and  $t > 0$  the time, we define as  $\rho(x, y, t)$  the pedestrian density (that has to stay non-negative and bounded:  $0 \leq \rho(\mathbf{x}, t) \leq \rho_{\max}$ ) and as  $u(\mathbf{x}, t)$  and  $v(\mathbf{x}, t)$  the  $x$ -component and  $y$ -component of the velocity vector  $\mathbf{v}$ , respectively. The model equations, along with their initial conditions, can be written as

$$\rho_t + \nabla \cdot (\rho \mathbf{v}) = 0, \quad (1)$$

$$(\rho \mathbf{v})_t + \nabla \cdot (\rho \mathbf{v} \otimes \mathbf{v} + P(\rho)) = \frac{1}{\tau} \rho (V(\rho) \vec{\mu} - \mathbf{v}); \quad (2)$$

$$\rho(\mathbf{x}, 0) = \rho_0(\mathbf{x}), \quad (3)$$

$$\mathbf{v}(\mathbf{x}, 0) = \mathbf{v}_0(\mathbf{x}), \quad (4)$$

where  $P(\rho)$  is an internal pressure function. In the momentum equations (2) the relaxation source term drives  $\mathbf{v}$  towards the desired speed  $V(\rho)\vec{\mu}$ , where  $V(\rho)$  is an equilibrium speed-density relation,  $\vec{\mu}$  is the desired direction vector, and  $\tau$  is a relaxation time.

For the speed-density relation we implement the following relation

$$V(\rho) = u_{\max} e^{-\alpha(\rho/\rho_{\max})^2}, \quad (5)$$

where  $\alpha > 0$  is a constant,  $u_{\max}$  is the free-flow velocity, and  $V(\rho_{\max}) \approx 0$  with  $\rho_{\max}$  being the congestion density at which the motion is hardly possible. The critical density, where the pedestrian flow is at a maximum, is given by  $\rho_{cr} = \rho_{\max}/\sqrt{2\alpha}$ . We note here that other equilibrium speed-density relations can also be implemented. For the internal pressure function we choose  $P(\rho) = \rho C_0^2$ , with  $C_0^2$  being constant representing, an anticipation factor.

With regard to the desired direction of motion  $\vec{\mu}$ , under the assumptions that pedestrians route choice is based on the shortest path to a destination and the avoidance of high density regions, following [15, 31, 32, 27, 26], we define a potential field  $\Phi$  that describes the instantaneous travel cost to a destination with  $\nabla\Phi = [\Phi_x, \Phi_y]^T$ , and set

$$\vec{\mu} = -\frac{\nabla\Phi}{\|\nabla\Phi\|} \quad (6)$$

The potential  $\Phi : \Omega \rightarrow \mathbb{R}$  is defined by the Eikonal equation

$$\|\nabla\Phi\| = \frac{1}{V(\rho)}, \quad t > 0, \quad \mathbf{x} \in \Omega, \quad (7)$$

$$\Phi = 0, \quad \mathbf{x} \in \Gamma_o, \quad \Phi = \infty, \quad \mathbf{x} \in \Gamma_w. \quad (8)$$

In simulations we assign a finite very large value for  $\Phi$  when  $\mathbf{x} \in \Gamma_w$ .

This choice for  $\vec{\mu}$  implies that pedestrians have a knowledge of the density distribution in the whole domain at each time instant, and use this to estimate their travel time. Such a reaction might be triggered, for example, by a global view on the pedestrian crowd or by information supplied by a real-time evacuation assistant.

Further, equations (1), (2) can be written in vector conservative form as,

$$\mathbf{Q}_t + \mathbf{F}(\mathbf{Q})_x + \mathbf{G}(\mathbf{Q})_y = \mathbf{S}(\mathbf{Q}), \quad (9)$$

where  $\mathbf{Q} = (\rho, \rho u, \rho v)^T$  and, the fluxes and sources are given as

$$\begin{aligned} \mathbf{F}(\mathbf{Q}) &= \begin{pmatrix} \rho u \\ \rho u^2 + \rho C_0^2 \\ \rho uv \end{pmatrix}, \quad \mathbf{G}(\mathbf{Q}) = \begin{pmatrix} \rho v \\ \rho uv \\ \rho v^2 + \rho C_0^2 \end{pmatrix}, \\ \mathbf{S} &= \begin{pmatrix} 0 \\ \frac{1}{\tau} \rho \left( -V(\rho) \frac{\Phi_x}{\|\nabla\Phi\|} - u \right) \\ \frac{1}{\tau} \rho \left( -V(\rho) \frac{\Phi_y}{\|\nabla\Phi\|} - v \right) \end{pmatrix}. \end{aligned} \quad (10)$$

The eigenvalues of the Jacobian matrices  $\mathbf{A}(\mathbf{Q}) = \frac{\partial \mathbf{F}}{\partial \mathbf{Q}}$  and  $\mathbf{B}(\mathbf{Q}) = \frac{\partial \mathbf{G}}{\partial \mathbf{Q}}$  are, respectively,

$$\lambda_1^A = u - C_0, \quad \lambda_2^A = u, \quad \lambda_3^A = u + C_0, \quad (11)$$

and

$$\lambda_1^B = v - C_0, \lambda_2^B = v, \lambda_3^B = v + C_0, \quad (12)$$

with their corresponding eigenvectors being linearly independent, i.e., the model is strictly hyperbolic. System (9) preserves its isotropic nature, meaning that information from all directions affect pedestrians' motion and this is the most distinct characteristic of this model. These are given as

$$\mathbf{e}_1^A = \begin{pmatrix} 1 \\ u - C_0 \\ v \end{pmatrix}, \mathbf{e}_2^A = \begin{pmatrix} 0 \\ 0 \\ 1 \end{pmatrix}, \mathbf{e}_3^A = \begin{pmatrix} 1 \\ u + C_0 \\ v \end{pmatrix}, \quad (13)$$

and

$$\mathbf{e}_1^B = \begin{pmatrix} 1 \\ u \\ v - C_0 \end{pmatrix}, \mathbf{e}_2^B = \begin{pmatrix} 0 \\ 1 \\ 0 \end{pmatrix}, \mathbf{e}_3^B = \begin{pmatrix} 1 \\ u \\ v + C_0 \end{pmatrix}. \quad (14)$$

## 2.2 Epidemic Spreading Model

The model utilized here is modified from [27] and is based on a PDE macroscopic version of a SEISV model where each type of pedestrian (SEIV) moves with the crowd speed  $\mathbf{v}$ , as this results from the crowd flow model. The density of each type of pedestrian satisfies then the following

$$\rho_t^S + \nabla \cdot (\rho^S \mathbf{v}) = \kappa \rho^I - \beta_I \rho^S - \xi \rho^S, \quad (15)$$

$$\rho_t^E + \nabla \cdot (\rho^E \mathbf{v}) = \beta_I \rho^S - \theta \rho^E, \quad (16)$$

$$\rho_t^I + \nabla \cdot (\rho^I \mathbf{v}) = \theta \rho^E - \kappa \rho^I, \quad (17)$$

$$\rho_t^V + \nabla \cdot (\rho^V \mathbf{v}) = \xi \rho^S, \quad (18)$$

where  $\rho^S, \rho^E, \rho^I$ , and  $\rho^V$  are densities of the susceptible, exposed, infected, and vaccinated/masked pedestrians, respectively, satisfying  $\rho = \rho^S + \rho^E + \rho^I + \rho^V$ . The model equations are supplied with relevant initial conditions  $\rho_0^S, \rho_0^E, \rho_0^I$  and  $\rho_0^V$ , similar to equations (1)–(4), satisfying  $\rho_0 = \rho_0^S + \rho_0^E + \rho_0^I + \rho_0^V$ . Further,  $\beta_I$  is the infection rate,  $\kappa$  is the recovery rate,  $\theta$  is the rate with which exposed persons are becoming infected, and  $\xi$  denotes vaccination rate. Pedestrians are potentially becoming exposed, when they are in contact with infected pedestrians. However, on the time scales under consideration,  $\kappa, \xi$  and  $\theta$  are very small, and thus, they are set to zero in our numerical simulations. Hence, the number of infected and vaccinated pedestrians remains constant, considering that there is no inflow of infected and vaccinated pedestrians at the boundary entries.

Here, we compute  $\beta_I = i_0 \beta(\mathbf{x}, t)$ , where  $\beta(\mathbf{x}, t)$  is the solution of the following drift-reaction-diffusion PDE in 2D following [27] as

$$\beta_t + \nabla \cdot (\beta \mathbf{U}_G) = \nabla \cdot (\sigma \nabla \beta) - \nu \beta + \frac{\rho^I}{\rho}, \quad (19)$$

with  $\beta(\mathbf{x}, 0) = 0$  as initial condition,  $\mathbf{U}_G = [u_G, v_G]^T$  a given velocity field of the surrounding air-flow in the computational region, and  $\sigma$  the effective turbulent viscosity for the aerosol. The term  $-\nu\beta$  models the fact that aerosol particles are settling due to the gravitational force [27, 37]. In this work we assume that  $\sigma$  is a constant equal to  $1.2 \cdot 10^{-3}$  [37, 27, 26] and we get the velocity field of the surrounding air-flow using potential flow theory, which will be described next. The parameter  $i_0$  is determined by the infectivity and is of  $O(10^{-2})$  [27, 26].

In this work, and in order to produce a steady velocity field  $\mathbf{U}_G$  of the surrounding air-flow in the computational region  $\Omega$  for model (19), it is assumed that the air flow is inviscid, incompressible, and irrotational [17]. Thus, the produced steady flow is governed by Laplace's equation as

$$\Delta\Psi = 0, \tag{20}$$

where  $\Psi(\mathbf{x})$  is the so-called velocity potential function. By implementing Neumann boundary conditions and imposing conditions on the derivative of the potential with respect to the normal direction (the derivative perpendicular to the boundary), we introduce air-flows for inflow and outflow boundaries imitating in such a way the inflows from ventilation ducts and outflows from exhaust ducts, respectively. Having computed the potential field we compute the resulting velocity field  $\mathbf{U}_G$  as

$$\mathbf{U}_G = \nabla\Psi. \tag{21}$$

### 3 Numerical Methodologies

The numerical approaches adopted here are based on the implementation of well-known conservative finite volume schemes to discretize model equations (9) for the crowd flow, equations (15)–(18) for the contagion model, and the advection part in equation (19) for the infection rate. Here we only give a brief presentation of them and we refer, for example, to the works in [19, 20, 9] for more details in hyperbolic PDEs and their numerical solution, and in [16] for crowd flow models in particular. To this end, the solution space  $(x, y, t)$  is split up into a uniform computational grid, where the grid spaces in the  $x$  and  $y$  directions are given by  $\Delta x$  and  $\Delta y$ , respectively and in time direction by  $\Delta t$ . The positions of the  $i$ th and  $j$ th nodes in the  $x$  and  $y$  directions, and  $n$ th node in time direction  $(x_i, y_j, t^n)$ , are given by  $(i\Delta x, j\Delta y, n\Delta t)$ , for  $i = 0, 1, \dots, N_x$  and  $j = 0, 1, \dots, N_y$ , with the solution vector, denoted as  $\mathbf{Q}_{i,j}^n$ , being defined at the center of the computational cell  $[x_{i-1/2,j}, x_{i+1/2,j}] \times [y_{i,j-1/2}, y_{i,j+1/2}]$ .

By doing so, the generic finite volume numerical scheme in 2D with explicit time integration can be written as

$$\mathbf{Q}_{i,j}^{n+1} = \mathbf{Q}_{i,j}^n - \frac{\Delta t}{\Delta x} [\mathbf{F}_{i+1/2,j}^n - \mathbf{F}_{i-1/2,j}^n] - \frac{\Delta t}{\Delta y} [\mathbf{G}_{i,j+1/2}^n - \mathbf{G}_{i,j-1/2}^n] + \Delta t \mathbf{S}_{i,j}^n, \tag{22}$$

where  $\mathbf{F}_{i\pm 1/2,j}^n$  and  $\mathbf{G}_{i,j\pm 1/2}^n$  are the numerical fluxes at the  $x$  and  $y$  (cell-boundary) directions, respectively. However, in our implementation, for model equations (9), we apply dimensional splitting by splitting the 2D problem into a sequence of two 1D problems along with a splitting technique between the advective part and the source terms of the model equations. This is performed as follows, along the  $x$ -direction

$$\begin{cases} \mathbf{Q}_{i,j}^* = \mathbf{Q}_{i,j}^n - \frac{\Delta t}{\Delta x} [\mathbf{F}_{i+1/2,j}^n - \mathbf{F}_{i-1/2,j}^n]; \\ \mathbf{Q}_{i,j}^{n+1/2} = \mathbf{Q}_{i,j}^* + \Delta t \mathbf{S}(\mathbf{Q}_{i,j}^*), \end{cases} \quad (23)$$

and along the  $y$ -direction

$$\begin{cases} \mathbf{Q}_{i,j}^{**} = \mathbf{Q}_{i,j}^{n+1/2} - \frac{\Delta t}{\Delta y} [\mathbf{G}_{i,j+1/2}^{n+1/2} - \mathbf{G}_{i,j-1/2}^{n+1/2}] \\ \mathbf{Q}_{i,j}^{n+1} = \mathbf{Q}_{i,j}^{**} + \Delta t \mathbf{S}(\mathbf{Q}_{i,j}^{**}). \end{cases} \quad (24)$$

For computing the numerical fluxes in (23) and (24) we implement the well-known approximate Riemann solver of Roe and we briefly describe it here. The idea behind Roe's scheme is to take a non-linear PDE system in quasi-linear form, e.g., in 1D

$$\mathbf{Q}_t + \mathbf{A}(\mathbf{Q})\mathbf{Q}_x = 0, \quad (25)$$

and linearize locally by approximating the Jacobian matrix(ces)  $\mathbf{A}(\mathbf{Q})$  at a computational cell's interface using Roe averages and in every time step repeat the process. For the purpose of this section we define  $\mathbf{Q}^R$  and  $\mathbf{Q}^L$  that represent the states on the right ( $R$ ) and left ( $L$ ) in the  $x$ -direction from the cell boundary interface ( $i \pm 1/2, j$ ). For a first-order accurate in space scheme, and for the  $(i, j)$ th cell,  $R \equiv (i + 1, j)$  and  $L \equiv (i, j)$ . Thus, the numerical flux is defined as

$$\mathbf{F}_{i+1/2,j}^{\text{Roe}}(\mathbf{Q}^L, \mathbf{Q}^R) = \frac{1}{2}[\mathbf{F}(\mathbf{Q}^L) + \mathbf{F}(\mathbf{Q}^R)] - \frac{1}{2}\tilde{\mathbf{R}}|\tilde{\mathbf{\Lambda}}|\tilde{\mathbf{R}}^{-1}[\mathbf{Q}^R - \mathbf{Q}^L]. \quad (26)$$

To obtain our approximated solution we write  $|\mathbf{A}|(\tilde{\mathbf{Q}}) = \tilde{\mathbf{R}}|\tilde{\mathbf{\Lambda}}|\tilde{\mathbf{R}}^{-1}$ , where  $\tilde{\mathbf{R}}$  is the (average) eigenvectors' matrix and  $\tilde{\mathbf{\Lambda}}$  is the diagonal matrix of the approximated (average) eigenvalues. Further, the Harten and Hyman [13, 19] entropy fix has been implemented, which modifies the approximated eigenvalues used in the Roe linearization by never allowing any eigenvalue to be too close to zero. In the same way the numerical fluxes  $\mathbf{G}_{i,j\pm 1/2}$  in the  $y$ -direction are also computed. For the crowd model (9) the Roe averages are

$$\tilde{\rho} = \sqrt{\rho^R \cdot \rho^L}, \tilde{u} = \frac{u^L \sqrt{\rho^L} + u^R \sqrt{\rho^R}}{\sqrt{\rho^R} + \sqrt{\rho^L}}, \tilde{v} = \frac{v^L \sqrt{\rho^L} + v^R \sqrt{\rho^R}}{\sqrt{\rho^R} + \sqrt{\rho^L}}, \quad (27)$$

and are used to compute the approximated eigenvalues (and eigenvectors) in  $\tilde{\mathbf{R}}$  and  $\tilde{\mathbf{\Lambda}}$ , as given in (11)–(14). A second-order spatial discretization can be obtained by properly defining the left ( $L$ ) and right ( $R$ ) states at the computational

cell interfaces. To this end, we utilize the classical Monotone Upstream-Centered Scheme for Conservation Laws (MUSCL) reconstruction technique; we refer, for example, in [9, 19]. Details about the MUSCL reconstruction are given in the Appendix.

For the boundary conditions here we implement the following at a layer of grid points (called ghost cells) around the computational domain.

- Free-slip at walls:  $\rho_g = \rho_i$ ,  $\mathbf{v}_g = \mathbf{v}_i - 2(\vec{\mathbf{v}}_i \cdot \vec{\mathbf{n}})\vec{\mathbf{n}}$ , with  $i$  being the neighbor point inside the domain and  $\vec{\mathbf{n}}$  the unit normal vector at a boundary cell.
- Outflow (at exits):  $\rho_g = \rho_i$ ,  $\vec{\mathbf{v}}_g = u_{\max}\vec{\mathbf{n}}$  (assuming on exits pedestrians can leave with maximum speed).
- Inflow boundary conditions can also be implemented e.g.  $\rho_g = \rho_{in}(\mathbf{x}, t)$ .

Finally, for the crowd flow model, and to numerically obtain the direction vector  $\vec{\mu}$  in the relaxation source term, we numerically solve the Eikonal equation (7), (8) at each time step implementing the Fast-Sweeping Method (FSM) of [38].

For each of the model equations (15)–(18) for the contagion model and the advection part in equation (19) we implement the well-known Rusanov numerical flux in scheme (22), again using the MUSCL reconstruction scheme, which reads, for example, in the  $x$ -direction as

$$\mathbf{F}_{i+1/2,j}^{\text{Rus}} = \frac{1}{2} [\bar{\mathbf{F}}(\bar{\mathbf{Q}}^R) + \bar{\mathbf{F}}(\bar{\mathbf{Q}}^L)] - \frac{C_{i+1/2,j}}{2} [\bar{\mathbf{Q}}^R - \bar{\mathbf{Q}}^L], \quad (28)$$

where  $\bar{\mathbf{F}}$  and  $\bar{\mathbf{G}}$  are the advection fluxes in (15)–(18) and (19),  $\bar{\mathbf{Q}}$  the relevant vector of unknowns, and  $C_{i+1/2,j} = \max\{|u^L|, |u^R|\}$ , i.e., the maximum absolute advection velocity in the  $x$ -direction at the computational cell interface. Similar is the formulation in the  $y$ -direction and the numerical fluxes  $\mathbf{G}_{i,j\pm 1/2}^{\text{Rus}}$ . Further, for the diffusion term  $\nabla \cdot (\sigma \nabla \beta)$  in equation (19), as well as for solving the Laplace equation (20), classical second-order central finite difference schemes are implemented [20].

Since the numerical solution of all models is obtained at each time node using the same time step  $\Delta t$ , their computation is stable under the global Courant-Friedrichs-Lewy (CFL) stability condition [19, 20] given as

$$\Delta t \leq \min \left( \frac{\text{CFL} \cdot \min\{\Delta x, \Delta y\}}{\max_{i,j} \{\|\mathbf{v}\|_{i,j} + C_0\}}, \frac{\text{CFL} \cdot \min\{\Delta x, \Delta y\}}{\max_{i,j} \{\|\mathbf{U}_G\|_{i,j}\}}, \frac{\Delta x^2 \Delta y^2}{2\sigma(\Delta x^2 + \Delta y^2)} \right), \quad (29)$$

where the first term in equation (29) stems from the Roe scheme, the second from the advective part of equation (19) using the Rusanov scheme, and the third from the discretization of the diffusion term of (19). The value of CFL = 0.8 was implemented in all simulations in Section 4 next.

**Remark.** There also exists another potential source of numerical instability for second-order crowd flow models with relaxation source terms present (and in general in PDEs having relaxation terms) when explicit integration methods are used.

Explicit methods may produce numerical instabilities when approximating the relaxation if the time step  $\Delta t$  is greater than the smallest intrinsic time scale of the system, see, e.g., [30]. In our case this results in satisfying that  $\Delta t < \tau$ , which is always true for all simulations presented next.

## 4 NUMERICAL TESTS AND RESULTS

In this section we present numerical simulations for evaluating the behavior of the model and, in particular, for evaluating the disease spreading under different conditions. Emphasis is given on the effect of certain parameters in the model, in particular we study the effect of the ventilation rates and direction of the resulting air-flow field, as well as we investigate the effect of variable maximum desired velocity  $u_{\max}$ , anticipation factor  $C_0$ , and of the presence of vaccinated/masked population. If not otherwise stated, we fix some of the parameters used in all the simulation scenarios presented below; these are  $\tau = 0.6$  s,  $\alpha = 7.5$ , and  $\rho_{\max} = 6$  ped/ $m^2$ , in the density-speed relation  $V(\rho)$ ,  $i_0 = 0.04$  (as in [27, 26]) for the infectivity rate, and  $\nu = 0.5$  in model (19) (i.e., we assume that 50% of the aerosol particles are settling due to gravitational forces). We compute the total number of pedestrians inside a facility, at each time instant, via relation  $R(t) = \int_{\Omega} \rho(\mathbf{x}, t) d\mathbf{x}$ .

### 4.1 Crowd Flow Towards an Exit

In this test we consider a closed room of size  $\Omega = [0, 10 \text{ m}] \times [0, 10 \text{ m}]$  with an exit 2 m wide at the right boundary centered at  $y = 5 \text{ m}$ . The initial density is  $\rho_0(\mathbf{x}) = 2.5$  ped/ $m^2$  in the region  $[1, 5] \times [2.5, 7.5]$ , leading to 50 people in this region, with  $\mathbf{v}_0(\mathbf{x}) = 0$  in the crowd flow model. Further, we set  $\rho_0^I = 0.25\rho_0$ , i.e., 25% of the pedestrians are considered infected, while initially  $\rho_0^E = 0$ . This test scenario is similar to one of the scenarios presented in [1, 18, 2]. The values of  $\Delta x$  and  $\Delta y$  were set equal to 0.05 m and the value of  $\Delta t = 2 \cdot 10^{-3}$  s.

In addition to studying the effect of ventilation air-flow field and of the presence of vaccinated/masked individuals to the percentage of total exposed individuals, we also study the effect of the desired speed  $u_{\max}$  and anticipation constant  $C_0$  in the internal pressure-like function. In particular, we compute the respective evacuation times and the corresponding total number of exposed individuals within this time interval. Empirical studies have shown that the average maximal reachable dimensionless velocity, i.e., the speed at which pedestrians walk when they are not hindered by others, is about 1.34 m/s with standard deviation of 0.37 m/s (see, for example, [7, 31]). However, due to impatience or in emergency situations people tend to move faster. To this end we consider two cases here, one with  $u_{\max} = 1.4$  m/s and one with  $u_{\max} = 2$  m/s. In Fig. 1 we present the behavior of the speed density relation for the two different maximum velocities where for both cases the critical density value for maximum pedestrian flow is obtained at  $\rho_{cr} = 1.549$  ped/ $m^2$ .

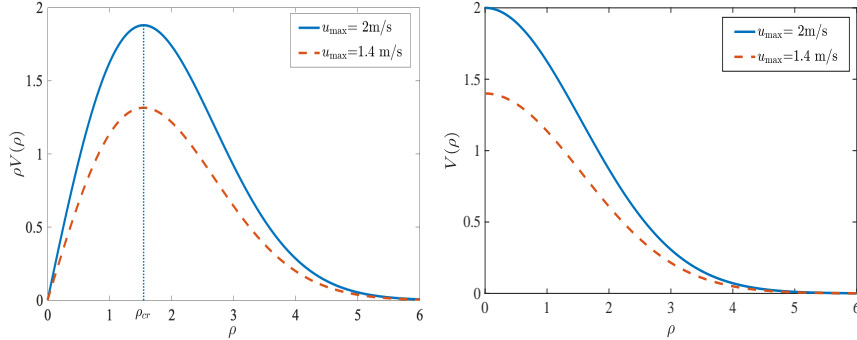


Figure 1: Equilibrium speed-density relations for flow (left) and velocity (right) for two different values of  $u_{\max}$ .

As for the anticipation constant  $C_0$ , which is a macroscopic indicator of the space concentration of crowd density, see, e.g., [22], smaller values of  $C_0$  correspond to pedestrians coming closer to each other (as, for example, in emergency situations), while larger values correspond to larger average distances between them. Here we consider three cases, as  $C_0 = 0.5, 0.8$ , and  $1.2$ .

#### 4.1.1 Effect of $u_{\max}$ , $C_0$ , and Vaccinated/Masked Population

Initially, we perform simulations in this test scenario, where we assume that there is no ventilation imposed in the facility. In Fig. 2 we present the total evacuation times for each value of  $C_0$  along with the predicted percentage of the exposed pedestrians when  $\rho_0^V = 0$ , i.e., with no masked/vaccinated pedestrians included. As it can be observed in Fig. 2, as the maximum desired velocity increases the total percentage of exposed pedestrians decreases, around between 3% and 5%, mainly as a result of the decreasing evacuation time, which is reasonably expected for increasing maximum speed. We note that, at an outflow boundary (exit) we keep track of the amount of exposed pedestrians that has exited the domain. As expected, after all pedestrians have exited the domain the total number of predicted exposed pedestrians remains constant in each case.

We further observe that as the anticipation factor increases the percentage of total exposed individuals decreases as a result of increasing average distances between individuals (dictated by the pressure function in the crowd flow model). Such an increase also results in a decrease in the evacuation time, which is explained as larger average distances between individuals may also lead to smoother overall flow, and thus, also, for example, to less evident clogging effects at the exit. This is evident also in Figs 3 and 4 where total density profile, infection coefficient profile, and exposed pedestrians' density, at different time instances with  $u_{\max} = 1.4 \text{ m/s}$ , are presented for two different values of  $C_0$ . Comparing the results in Figs 3 and 4 we see that for smaller values of  $C_0$ ,

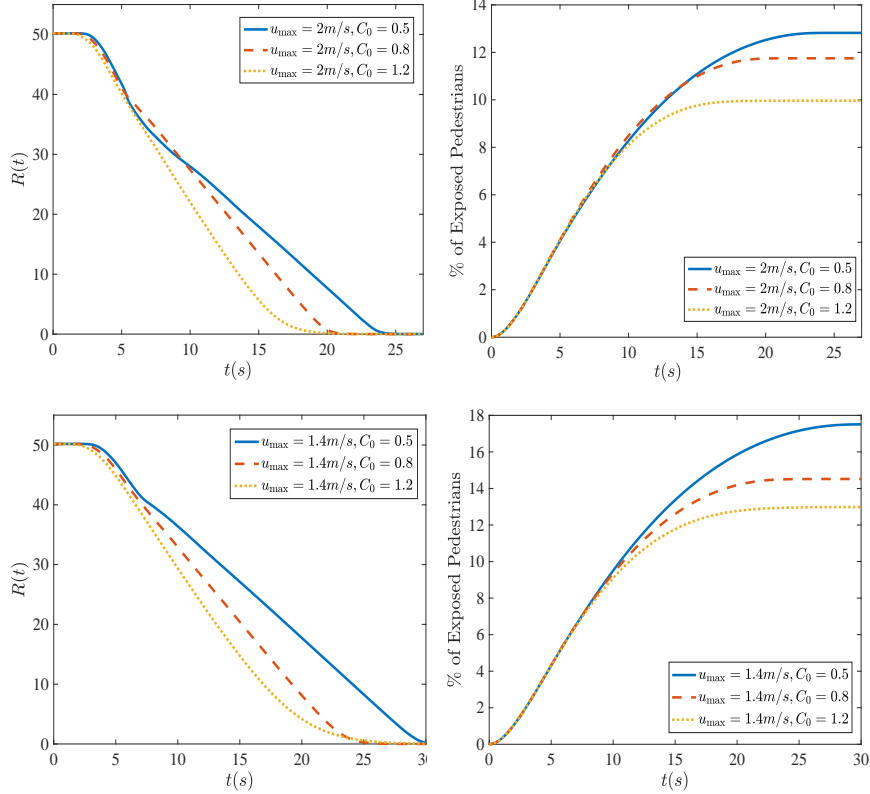


Figure 2: Time evolution of the total number of pedestrians  $R(t)$  (left) and percentage of exposed pedestrians (right) with  $u_{\max} = 2 \text{ m/s}$  (top) and  $u_{\max} = 1.4 \text{ m/s}$  (bottom), for three different values of  $C_0$  with  $\rho_0^V = 0$ .

i.e., allowing smaller distances between pedestrians, causes stronger interactions and formation of inhomogeneities in the density distribution and, as a result, we observe much higher densities, especially near the exit, which persist in time. On the other hand, increasing the value of  $C_0$ , higher repelling forces between pedestrians prevent high densities and formation of inhomogeneities in the density distribution, allowing for a smoother and faster evacuation. Further, in Figs 3 and 4, we can observe the evolution of the infection coefficient  $\beta^I$  that follows the pedestrians' movement and, at the same time, spreads in the domain, due to diffusion effects as given in model (19).

Next, in Fig. 5 we present the same simulations but now assuming that 15% of the pedestrians are masked or vaccinated, i.e.,  $\rho_0^V = 0.15\rho_0$ . The effect of incorporating masked/vaccinated individuals is a decrease in the total number of exposed individuals, which is reasonably expected. Comparing with the percentage of exposed pedestrians in Fig. 2, a decrease of about 2-5% is observed.

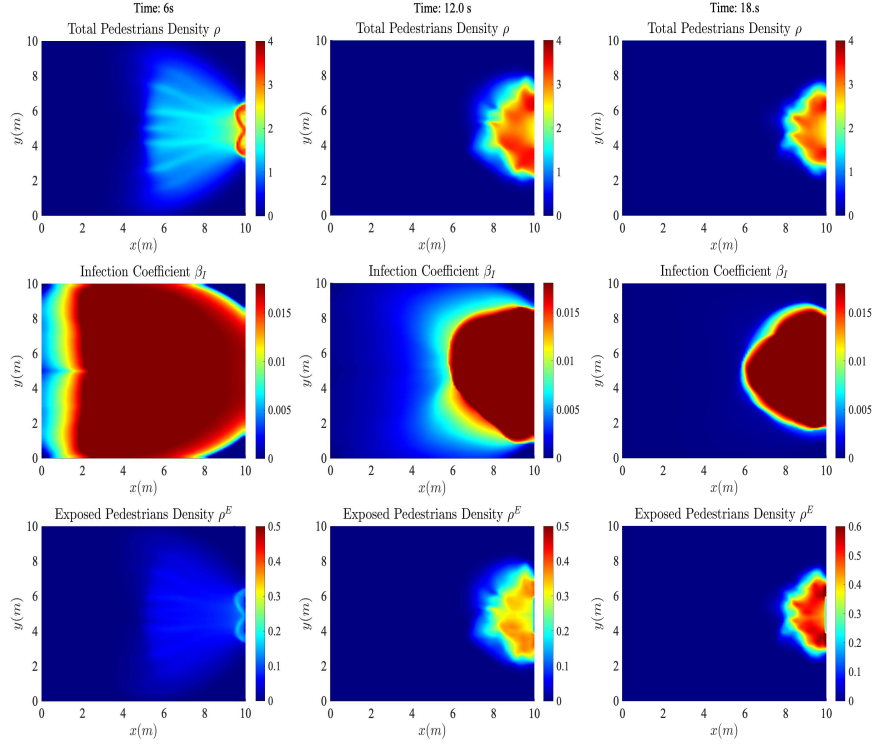


Figure 3: Total density profiles (top), infection coefficient profile (middle) and exposed pedestrians' profile at different time instances with  $u_{\max} = 1.4 \text{ m/s}$ ,  $C_0 = 0.5$ , with no ventilation and  $\rho_0^V = 0$ .

#### 4.1.2 Effect of Different Ventilation Air-Flow Rates and Directions

To study the effect of ventilation imposed in the room, we assume one case with an inflow ventilation duct at the middle of the left boundary and one exhaust duct at the middle of the right boundary, both being  $2 \text{ m}$  wide, producing an air-flow field along the pedestrians motion towards the exit. The second case reverses the position of inflow and outflow ducts producing an air-flow field against the pedestrians' motion. To produce the steady velocity field  $\mathbf{U}_G$  from (21), in the first case, the derivative of the potential  $\Psi$  normal to the ventilation boundaries was set equal to  $\mathbf{u}_{in} = [u_{in}, 0]^T$  for the left boundary and  $\mathbf{u}_{out} = [-u_{in}, 0]^T$  for the right boundary, as to introduce the air-flow in the computational domain. The opposite is done for the second case. We consider

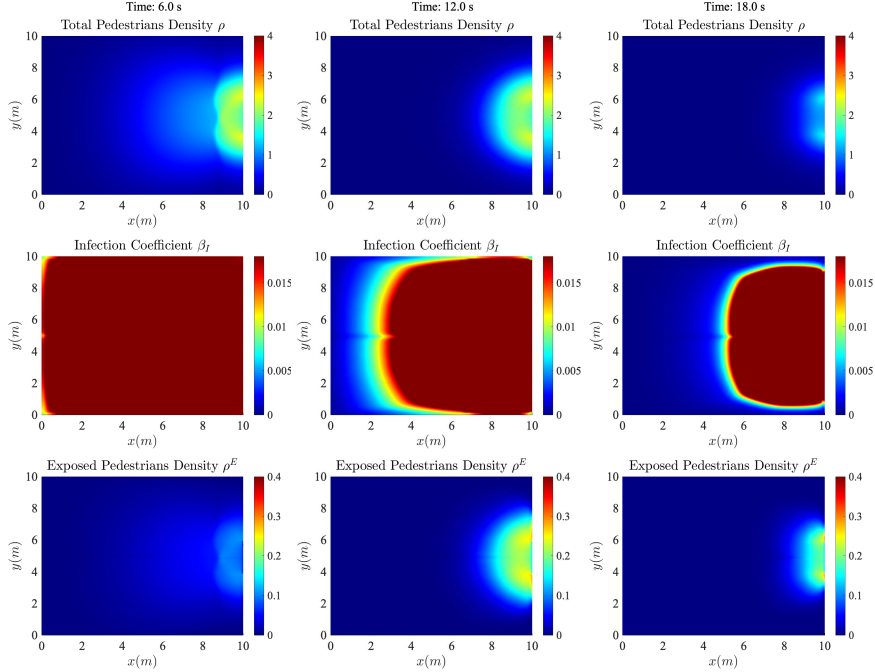


Figure 4: Total density profiles (top), infection coefficient profile (middle) and exposed pedestrians' profile at different time instances with  $u_{\max} = 1.4 \text{ m/s}$ ,  $C_0 = 1.2$ , with no ventilation and  $\rho_0^V = 0$ .

two settings for the ventilation speed, one with  $u_{in} = 5 \text{ m/s}$ , and one with  $u_{in} = 10 \text{ m/s}$  (that are practically realistic values, see, e.g., [5]). The resulting air-flow fields in both cases, along the pedestrian's motion and against it, are shown in Fig. 6 for  $u_{in} = 10 \text{ m/s}$ .

In Figs 7 and 8 we present, respectively, with ventilation along and against the pedestrians' flow direction, the total pedestrians' density profiles, infection coefficient profile, and exposed pedestrians' profile at different time instances for  $u_{\max} = 1.4 \text{ m/s}$ ,  $C_0 = 1.2$ , and  $u_{in} = 10 \text{ m/s}$ . Although the evolution of the total pedestrians' movement is the same in each case, significant differences can be observed in the evolution of the infection coefficient in the room, affected by the air-flow fields, and, as a result, in that of the predicted exposed pedestrians. In particular, we observe from Fig. 8 that people in this case, with air-flow against pedestrians' direction, move at locations where the values of  $\beta^I$  is smaller, which is a result of air being cleaner at locations close to the inlet ventilation duct; while the opposite is true in the case where the air-flow is along their direction, as in Fig. 7. Further, since there exists a significant congestion

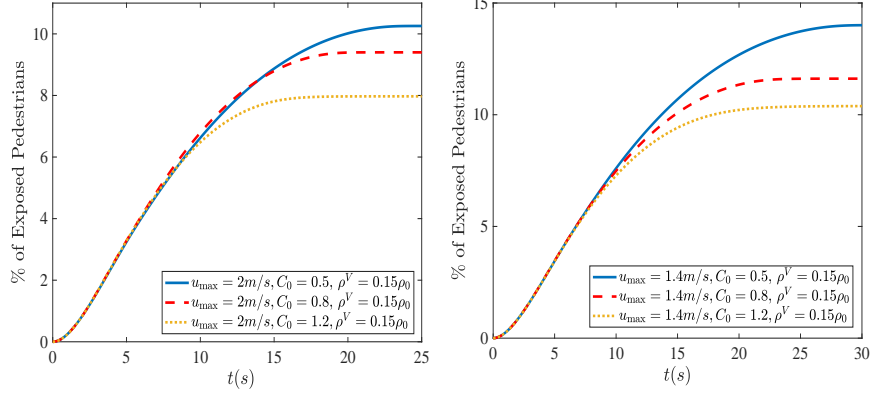


Figure 5: Time evolution of the percentage of exposed pedestrians with  $u_{\max} = 2\text{ m/s}$  (left) and  $u_{\max} = 1.4\text{ m/s}$  (right), for three different values of  $C_0$  for  $\rho_0^V = 0.15\rho_0$ .

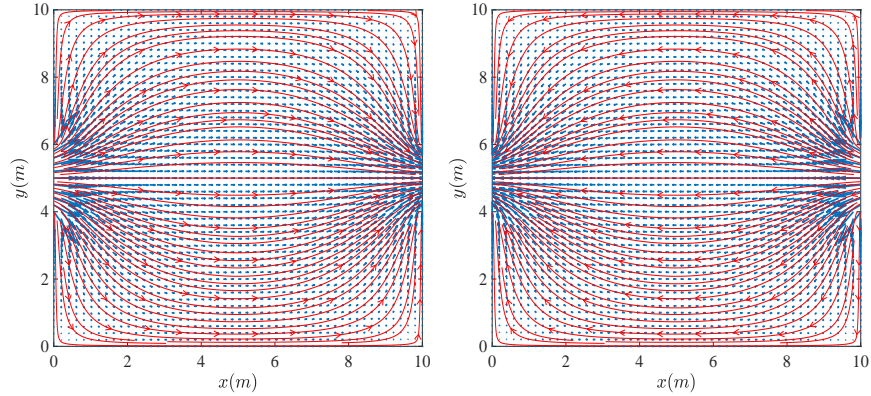


Figure 6: Velocity field  $\mathbf{U}_G$  vectors (in blue) and the corresponding streamlines for a ventilated room along the pedestrians' moving direction (left) and against (right) for  $u_{in} = 10\text{ m/s}$ .

(clogging) near the exit, especially for smaller values of  $C_0$ , this “pocket” of clean air near the exit is expected to have a profound effect in the number of exposed pedestrians. This observation is also consistent with, for example, [25].

Indeed, the results as shown in Figs 9-12 for the two different values of  $u_{\max}$  (that include also the effect of masked/vaccinated individuals) verify this. More precisely, first we observe that the number of exposed individuals decreases with increasing ventilation rate, which is reasonably expected. In particular, as model (19) predicts, increasing ventilation rate results in a larger area of smaller

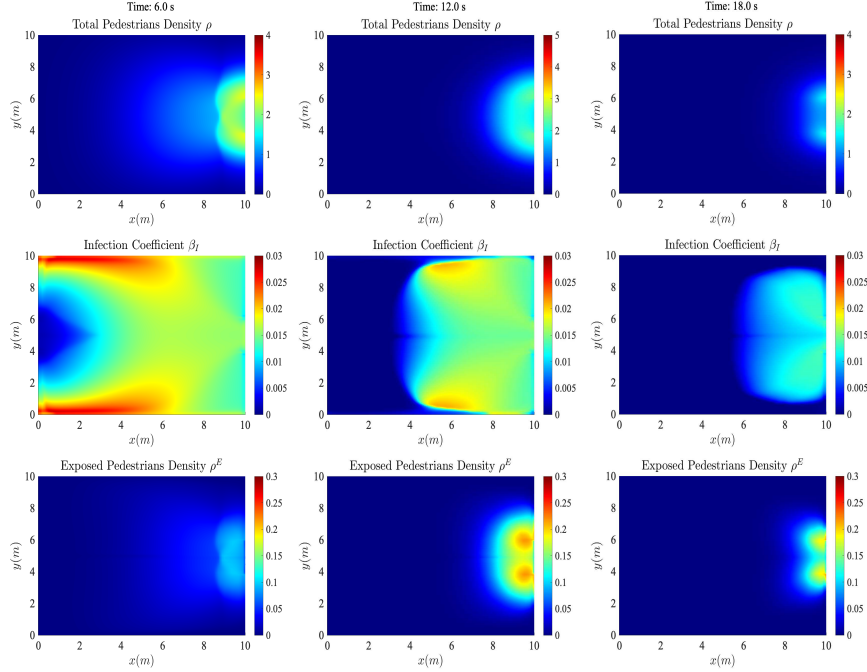


Figure 7: Total density profiles (top), infection coefficient profile (middle), and exposed pedestrians' profile at different time instances with  $u_{\max} = 1.4 \text{ m/s}$ ,  $C_0 = 1.2$ , and ventilation along the pedestrians' flow direction with  $u_{in} = 10 \text{ m/s}$ .

average values for the  $\beta^I$  coefficient, which describes the degree of infection transmission. Comparing the results presented in Figs. 9 and 11 with the results presented in Fig. 2 there is a significant decrease, up to 6% in the expected number of exposed pedestrians. In all cases it can be observed that the number of exposed individuals decreases when people move against the ventilation air-flow field in this test case. The same can be concluded if one compares Figs 10 and 12 with Fig. 5 when a small percentage of vaccinated/masked pedestrians is included. In this case, the percentage of exposed pedestrians reaches its lowest value, of approximately 4% of the total number of pedestrians, when  $C_0 = 1.2$  and  $u_{\max} = 2 \text{ m/s}$ , while it is approximately 7% when  $C_0 = 1.2$  and  $u_{\max} = 1.4 \text{ m/s}$ , both for an induced air-field against the pedestrians' movement with  $u_{in} = 10 \text{ m/s}$ .

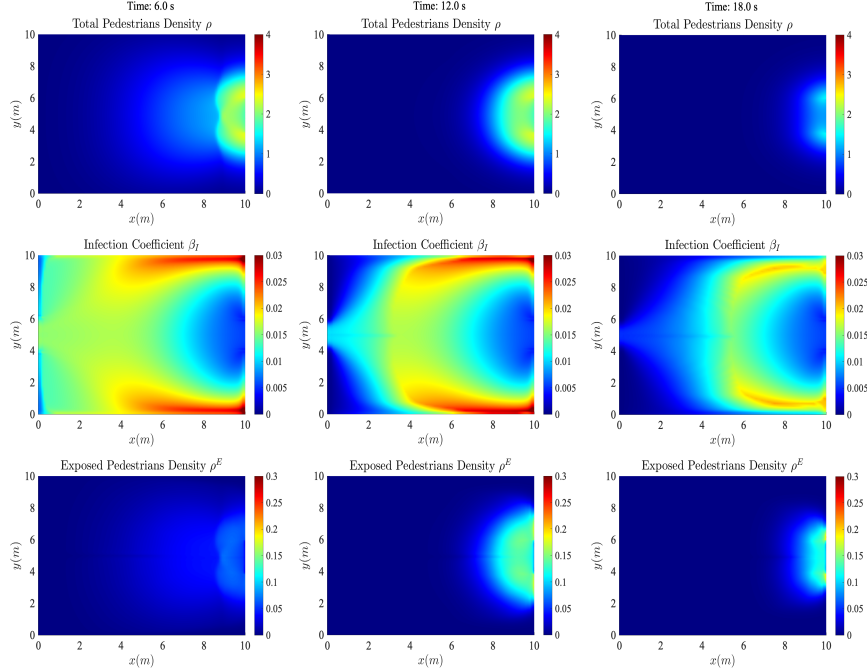


Figure 8: Total density profiles (top), infection coefficient profile (middle), and exposed pedestrians' profile at different time instances with  $u_{\max} = 1.4 \text{ m/s}$ ,  $C_0 = 1.2$ , and ventilation against the pedestrians' flow direction with  $u_{in} = 10 \text{ m/s}$ .

## 4.2 Crowd Flow Towards Two Exits

Here we consider again a closed room of size  $\Omega = [0, 10 \text{ m}] \times [0, 10 \text{ m}]$  but now with two exits, each being  $2 \text{ m}$  wide at the right boundary centered at  $y = 3 \text{ m}$  and  $y = 8 \text{ m}$ . The initial density is  $\rho_0(\mathbf{x}) = 2.5 \text{ ped/m}^2$  in the region  $[1, 5] \times [2.5, 7.5]$ , leading again to 50 people in this region, with  $\mathbf{v}_0(\mathbf{x}) = 0$ . Further,  $\rho_0^I = 0.25\rho_0$ , while initially  $\rho_0^E = 0$ . In this test scenario we mainly focus on the effect of adding an extra exit (along with the exits' location), as well as on the effect of the direction of the imposed air-flow field.

First, from Figure 13, where the time evolution of pedestrians and percentage of exposed pedestrians with  $u_{\max} = 2 \text{ m/s}$  and  $u_{\max} = 1.4 \text{ m/s}$  for three different values of  $C_0$  are presented, we observe that, in this two-exit case, the evacuation time, and consequently, the total number of exposed individuals, are significantly reduced when compared with the results for the one exit scenario in Fig. 2. However, the effect of variable pressure coefficient  $C_0$  is less evident, in comparison with the case of a single exit. This can be explained by the fact that

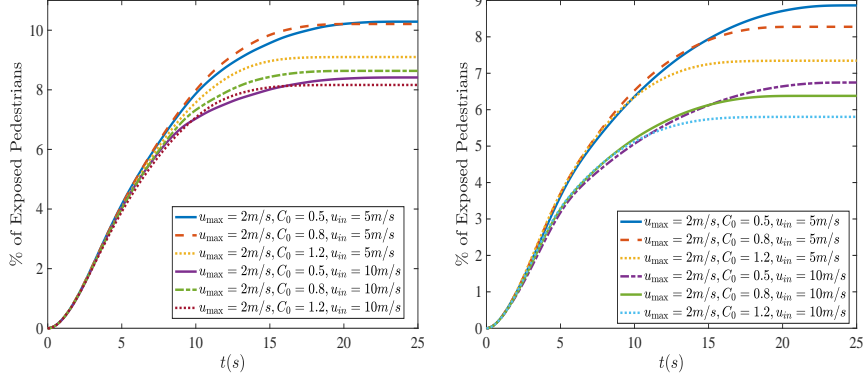


Figure 9: Percentage of exposed pedestrians in a ventilated room for two different ventilation speeds, along the pedestrians' direction (left) and against (right,) with  $\rho_0^V = 0$  and  $u_{\max} = 2 \text{ m/s}$ .

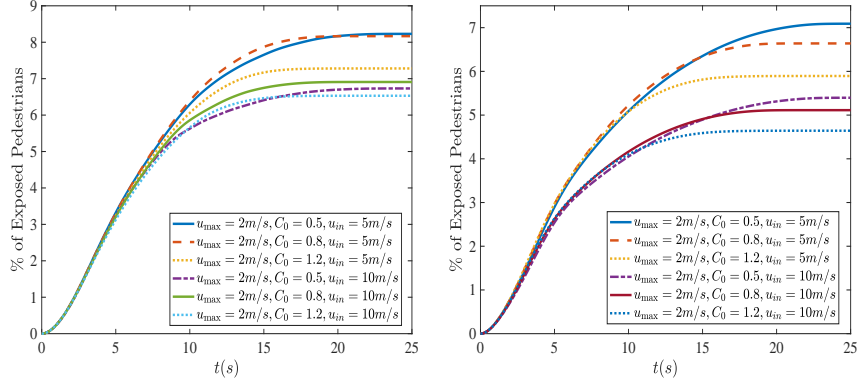


Figure 10: Percentage of exposed pedestrians in a ventilated room for two different ventilation speeds, along the pedestrians' direction (left) and against (right,) with  $\rho_0^V = 0.15\rho_0$  and  $u_{\max} = 2 \text{ m/s}$ .

two exits increase the capacity flow (i.e., the maximum discharge flow) at the exits of the space considered, and thus, larger outflows can be accommodated, which in turn implies that a clogging (i.e., a congestion) phenomenon may be avoided even for smaller average distances between pedestrians (that may imply a larger outflow at the exits). In addition, since pedestrians are roughly split into two groups (towards each exit as shown, for example, in Fig. 14) smaller densities are observed (i.e., smaller numbers of people within a certain area), and thus, increasing the pressure coefficient to impose stricter average distances between people does not have a significant effect on spreading. Further in this case, the effect of the increase in the maximum allowable speed  $u_{\max}$  to  $2 \text{ m/s}$

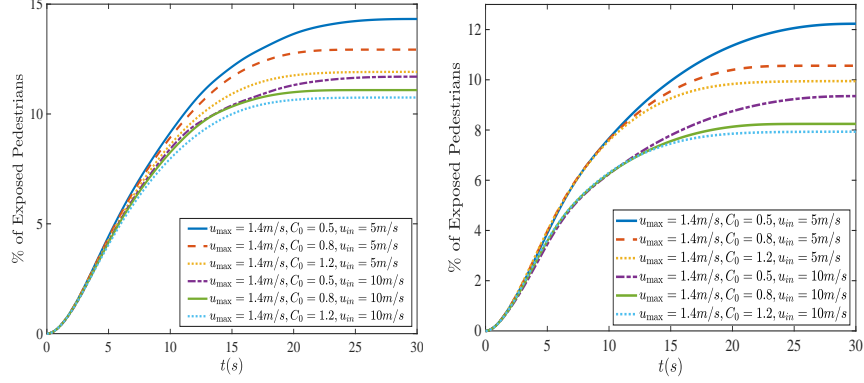


Figure 11: Percentage of exposed pedestrians in a ventilated room for two different ventilation speeds along the pedestrians' direction (left) and against (right), with  $\rho^V = 0$  and  $u_{\max} = 1.4 \text{ m/s}$ .

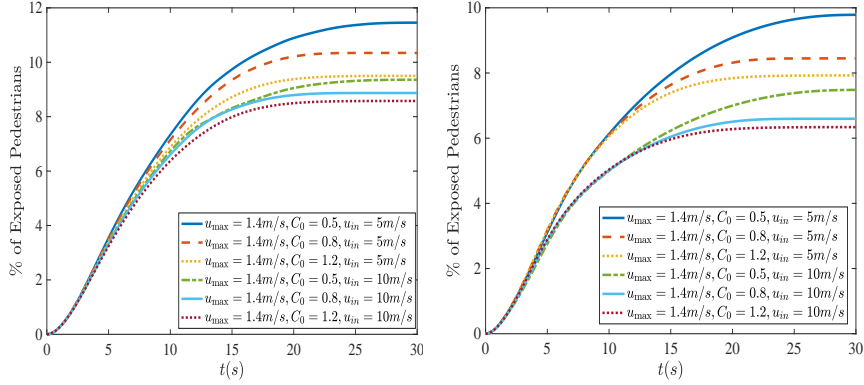


Figure 12: Percentage of exposed pedestrians in a ventilated room for two different ventilation speeds along the pedestrians' direction (left) and against (right), with  $\rho^V = 0.15\rho_0$  and  $u_{\max} = 1.4 \text{ m/s}$ .

when compared to that of  $1.4 \text{ m/s}$  can be clearly seen, in terms of a reduced evacuation time and a lower percentage of exposed individuals. In Fig. 14, where we show total density profile, infection coefficient profile, and exposed pedestrians' density, at different time instances with  $u_{\max} = 1.4 \text{ m/s}$  for  $C_0 = 0.5$ , we can observe the evolution of the infection coefficient  $\beta^I$  that follows the pedestrians' movement towards the two exits. For this value of  $C_0$  some strong interactions and formation of inhomogeneities in the density distribution are still evident.

Next, in this two-exit case, we focus on the effect of imposing the two ventilation scenarios as in Section 4.1.2 for the case  $u_{\max} = 1.4 \text{ m/s}$ , for which

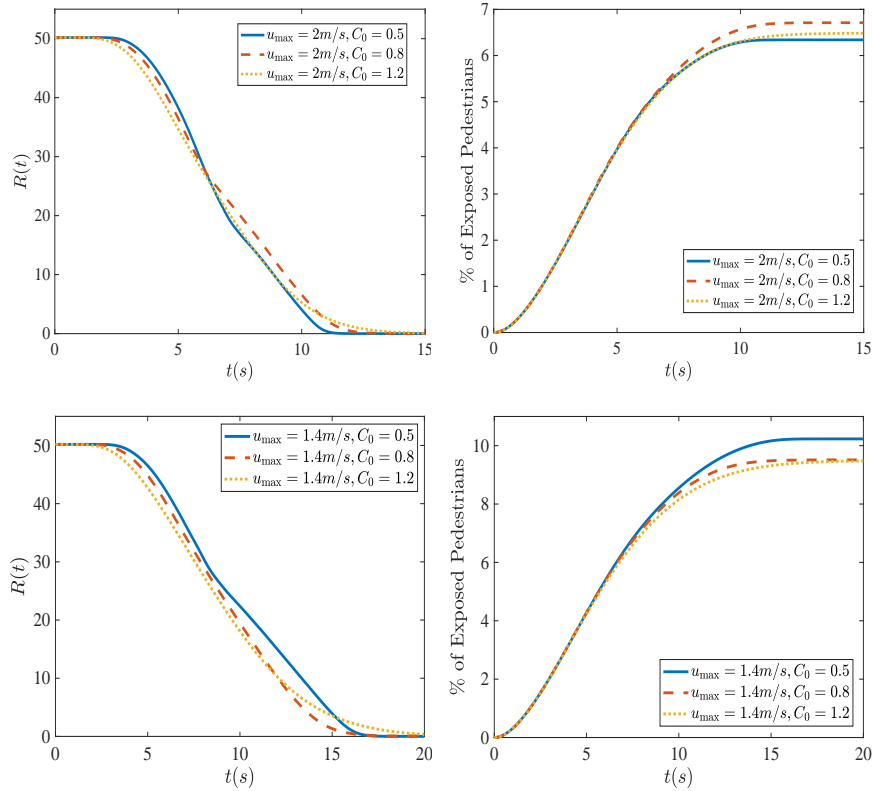


Figure 13: Two exits: Time evolution of the total number of pedestrians  $R(t)$  (left) and percentage of exposed pedestrians (right) with  $u_{\max} = 2 \text{ m/s}$  (top) and  $u_{\max} = 1.4 \text{ m/s}$ , for three different values of  $C_0$ .

the exposed pedestrians' number is in general larger, and  $u_{in} = 10 \text{ m/s}$  in the ventilation. Initially we present, as indicative results, in Figs 15 and 16, the total pedestrians' density profiles, infection coefficient profile, and exposed pedestrians' profile at different time instances for air-flow along and against the pedestrians' flow direction for  $C_0 = 0.5$ . From Fig. 17 we observe that an increasing ventilation rate in general implies smaller percentages of exposed individuals, which is reasonably expected. However, the relevant improvement with respect to the no ventilation case is not as significant as in the case of one exit, at least for low ventilation rates. This can be explained by the fact that, in the case of two exits, the evacuation time is roughly half of the respective evacuation time in the one-exit case. This in turn implies that large ventilation rates may not result in significant improvements with respect to spreading as pedestrians exit the space fast enough. Still, when compared with the obtained results in Fig. 13, when ventilation is not imposed, one can observe a 3-4% decrease in the number of exposed individuals, in the case of an imposed air-flow

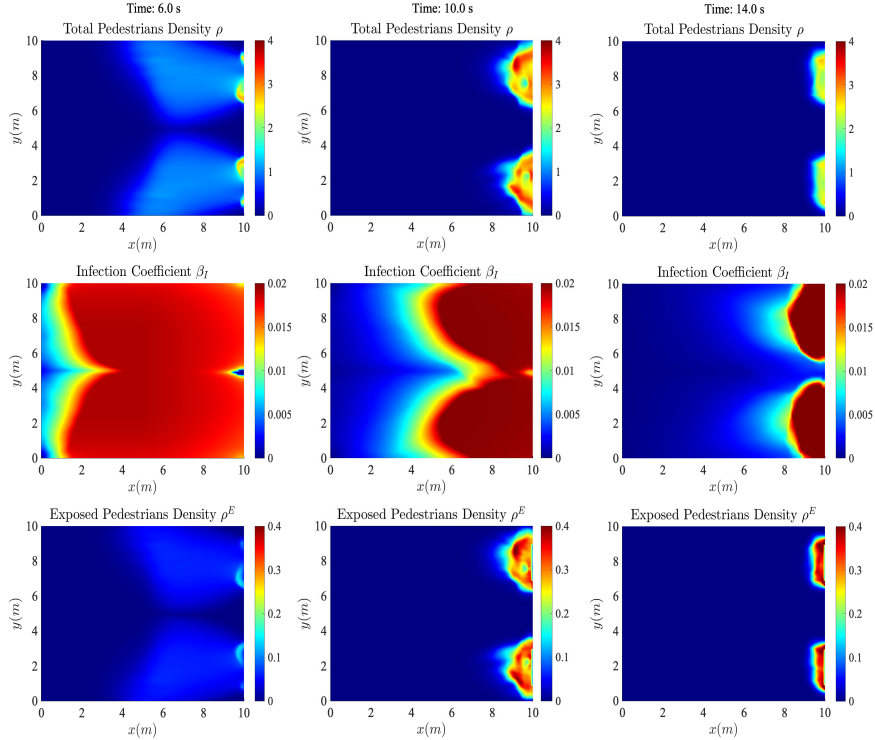


Figure 14: Two exits: Total density profiles (top), infection coefficient profile (middle), and exposed pedestrians' profile at different time instances with  $u_{\max} = 1.4 \text{ m/s}$ ,  $C_0 = 0.5$ , and no ventilation.

against the pedestrians direction for  $u_{in} = 10 \text{ m/s}$ . We also note here that, while the ventilation ducts (for both cases of the air-flow field) are placed at the middle of the right (exit) boundary, pedestrians are directed to two exits that are relatively far from these. In return it is expected that the effect of the imposed ventilation will be less profound as compared with the respective case in Section 4.1.2.

### 4.3 Large Crowd Flow Towards an Exit

With this test case we aim to investigate the performance of the model in the case of a larger number pedestrians moving in larger spaces/distances. Our main target here is to study the effect of different ventilation patterns induced in the facility. To this end, we consider a walking facility of size  $\Omega = [0, 50 \text{ m}] \times [0, 20 \text{ m}]$  with an exit at the right boundary centered at  $y = 10 \text{ m}$ . The initial density is

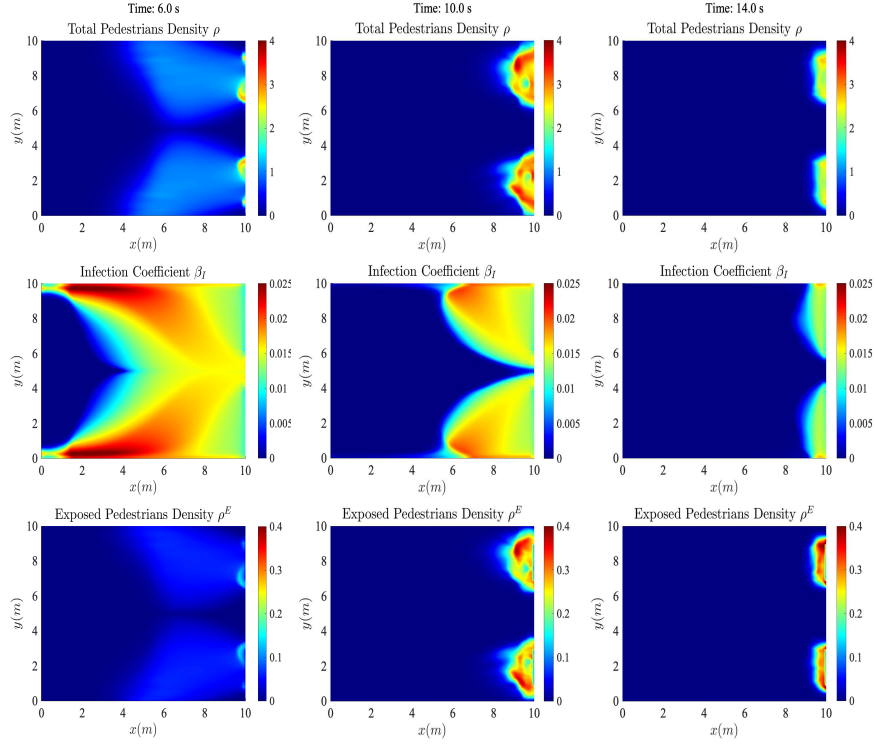


Figure 15: Two exits: Total density profiles (top), infection coefficient profile (middle), and exposed pedestrians' profile at different time instances with  $u_{\max} = 1.4m/s$ ,  $C_0 = 0.5$ , and with ventilation air-flow field along the pedestrians' flow direction with  $u_{in} = 10 m/s$ .

$\rho_0(\mathbf{x}) = 1 \text{ ped}/m^2$  in the region  $[0, 20] \times [0, 20]$ , leading to around 400 people in this region, with  $\mathbf{v}_0(\mathbf{x}) = 0$ . Further, we set  $\rho_0^I = 0.1\rho_0$ , while initially  $\rho_0^E = 0$  and  $\rho_0^V = 0$ . In this case we fix the value of  $u_{\max}$  to  $1.4m/s$ . The values of  $\Delta x$  and  $\Delta y$  were set to 0.1 and the value of  $\Delta t$  to  $5 \cdot 10^{-3}$ .

Initially, we compare the effect of the size of the exit for the three different values of  $C_0$  as shown in Fig. 18, in terms of the exiting time, as well as the percentage of the exposed pedestrians predicted. We assume first an exit 6 m wide and then one 4 m wide, both for  $u_{\max} = 1.4 m/s$  and no ventilation present. As it was expected in this setup, the evacuation time is much larger for the smaller exit, for all values of  $C_0$ . This leads to an increase of the predicted percentages of exposed pedestrians, especially for the case of  $C_0 = 0.5$  where an approximately 10% increase can be observed while for  $C_0 = 1.2$  the increase is approximately 5%, as compared with the case of an exit 6 m wide.

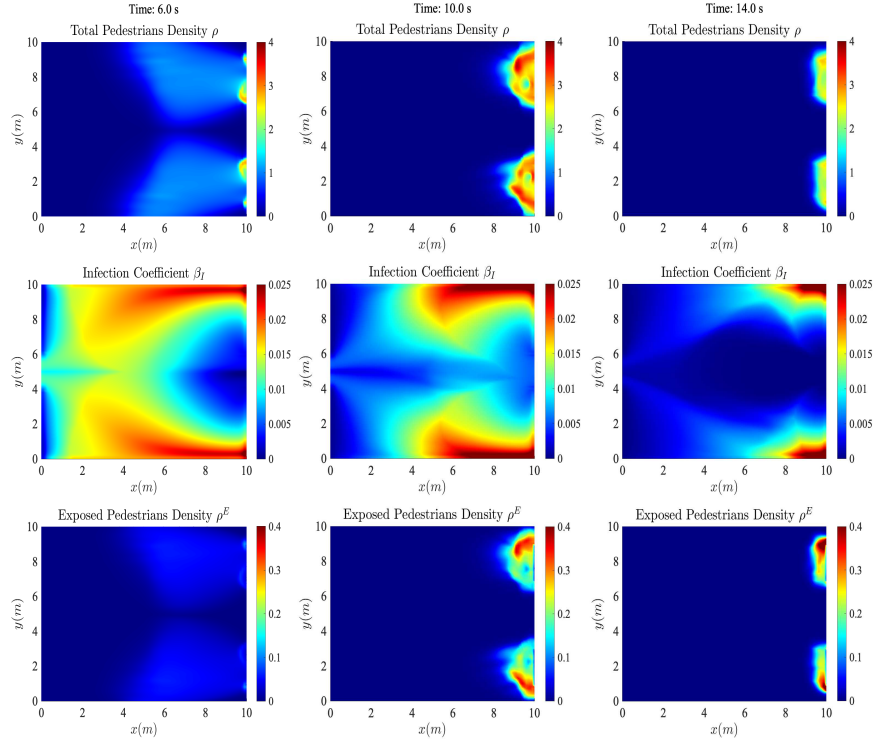


Figure 16: Two exits: Total density profiles (top), infection coefficient profile (middle), and exposed pedestrians' profile at different time instances with  $u_{\max} = 1.4m/s$ ,  $C_0 = 0.5$ , and with ventilation air-flow filed against the pedestrians' flow direction with  $u_{in} = 10 m/s$ .

The effect of imposing different values of  $C_0$  is given in Figs 19 and 20 for the 4 m exit, where total density profile, infection coefficient profile, and exposed pedestrians' density at different time instances are shown. Again, the effect of the internal pressure function that describes the repelling forces between individuals and prevents or not from overcrowding is evident. We can observe, also in this case, that for the smaller value of  $C_0$  there is a significant decrease of the outflow of pedestrians through the exit, which essentially means that the clogging phenomenon persists more in time. On the other hand, increasing  $C_0$  leads to a less pronounced congestion effect and the outflow is smoother leading to smaller densities and faster evacuation times, and thus, to spreading mitigation.

In the following simulations we focus our interest on the case of a 4m wide exit, which is the case that corresponds to the worst-case scenario, in terms of

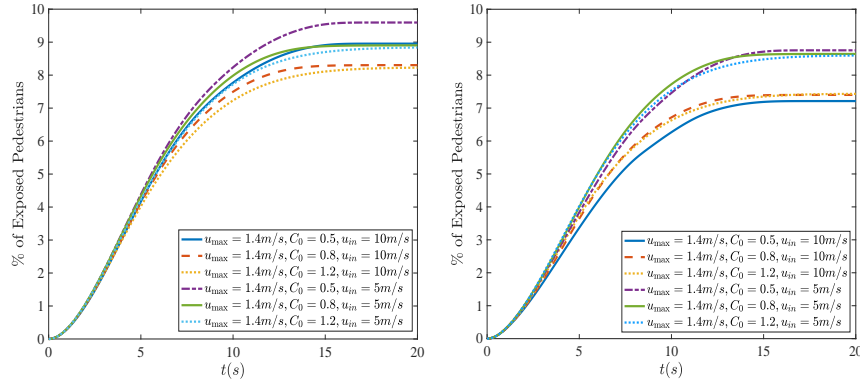


Figure 17: Two exits: Percentage of exposed pedestrians in a ventilated room for two different ventilation speeds along the pedestrians’ direction (left) and against (right) with  $\rho_0^V = 0$  and  $u_{max} = 1.4$  m/s.

the predicted number of exposed pedestrians for all values of  $C_0$ . Due to the larger scale of the facility, we impose two inflow ventilation ducts at the middle of the top and bottom boundaries and two exhaust ducts at the middle of the right and left boundaries, all being 8 m wide, as shown in Fig. 21 (top) and we call the obtained velocity field air-flow pattern I. Then we consider the reverse case called air-flow pattern II as shown in Fig. 21 (bottom). In both patterns, we consider the ventilation speed to be  $u_{in} = 10$  m/s and  $u_{out} = -10$  m/s. The results obtained, for the two air-flow patterns, in terms of the percentage of the exposed pedestrians for each value of  $C_0$  are presented in Fig. 22 and compared with the no ventilation case. As it can be observed for the case of  $C_0 = 0.5$ , both ventilation patterns reduce the amount of the predicted exposed individuals, with air-flow pattern I resulting to an almost 10% drop, as compared with the no ventilation case. A moderate drop of the expected exposed pedestrians can be observed in the case of  $C_0 = 1.2$ .

Referring now to Fig. 23 and Fig. 24 we observe that for such situations, where crowd occupies a large space for long time at the vicinity of the exit, pattern II leads to higher degree of spreading because infection coefficient is produced and advected inside the domain, thus affecting a large portion of the crowd that is concentrated in a large area, of about 10 meters, near the exit. In contrast, pattern I causes the infection coefficient to exit the domain more efficiently, or, in other words, pattern I cleans the air at a large area near the exit more efficiently, thus leading to smaller numbers of exposed individuals, due to imposing cleaner air near the exit. This is not in contradiction with the results of Sections 4.1 and 4.2, because the “pocket” of clean air reported there, in the case of ventilation field against the pedestrians direction, which resembles more pattern II than pattern I, may be still evident, nevertheless that pocket is concentrated at a very small area around the exit that does not have any benefit

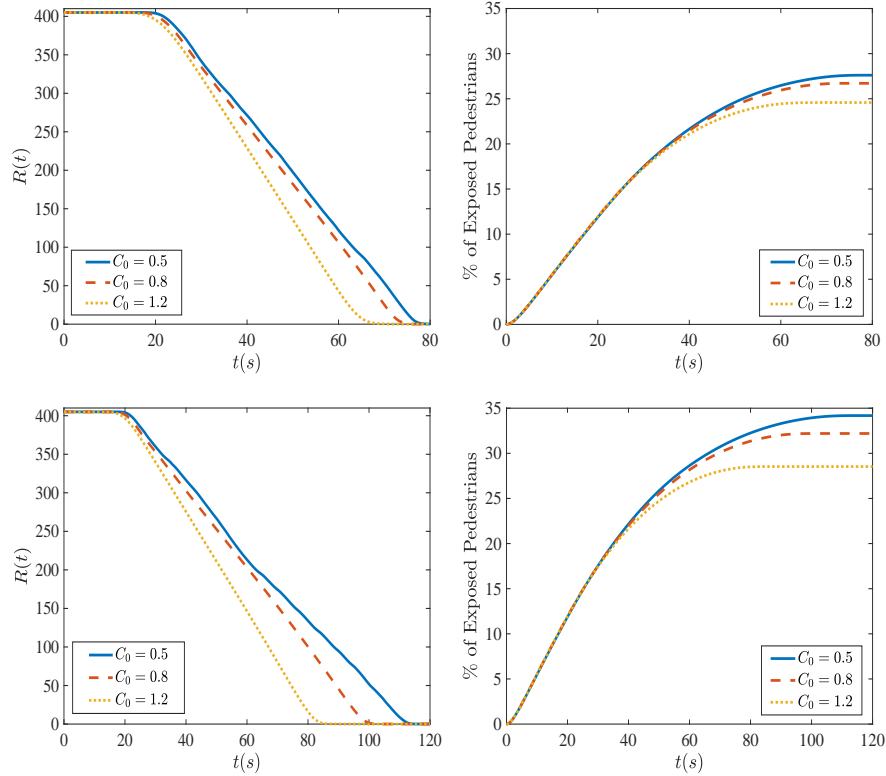


Figure 18: Corridor: Time evolution of the total mass  $R(t)$  of pedestrians (left) and percentage of exposed pedestrians (right) with  $u_{\max} = 1.4 \text{ m/s}$ , for three different values of  $C_0$ , with one exit 6 m wide (top) and 4 m wide (bottom), with no ventilation.

in the present case, where the crowd occupies a much larger area around the exit.

## 5 Conclusions and Recommendations

In this paper, we performed several numerical investigations for studying the effect of employment of different, epidemics transport control measures, in scenarios in which pedestrians occupy and evacuate closed spaces. In particular, we performed tests varying the ventilation rate and direction, the maximum speed of pedestrians, and the average distances between pedestrians, as well as incorporating in the crowd masked or vaccinated individuals. We also studied the effect of increasing the size or number of the exits. The tests performed employing a macroscopic PDE model consisting of three main components, namely, a crowd flow dynamics component, an epidemics transport dynamics component,

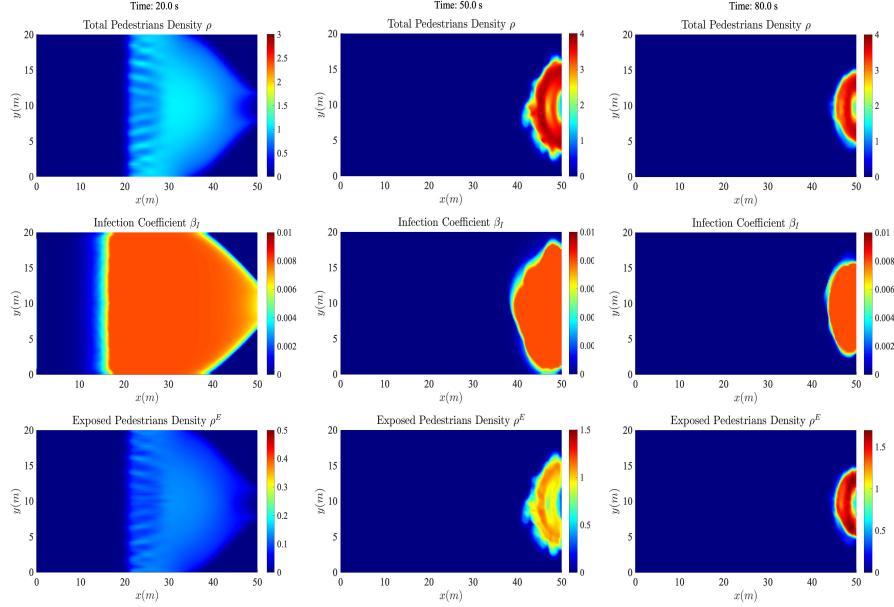


Figure 19: Corridor with a 4  $m$  exit: Total density profiles (top), infection coefficient profile (middle), and exposed pedestrians' profile at different time instances with  $u_{\max} = 1.4 \text{ m/s}$ ,  $C_0 = 0.5$ , and with no ventilation.

and an equation for computing the infection coefficient.

Based on the results of the tests, we observed the following. Increasing the pressure coefficient  $C_0$  leads, in general, to lower degree of spreading, as it leads to higher average distances between pedestrians, and thus, to a smoother crowd flow with less evident congestion/clogging effects at the exit (where the spreading is more profound). However, the effect of increasing  $C_0$  may be less evident in situations where the capacity of the outflow at the exit is sufficiently large (e.g., due to multiple or large exits), as, in such scenarios, pedestrians may exit the domain keeping sufficiently high, average distances. Increasing the maximum speed coefficient  $u_{\max}$  leads, in general, to lower degree of spreading, as it results in smaller evacuation times. However, very large values of  $u_{\max}$  may result in higher spreading when the outflow capacity at the exits is not sufficiently large, as it may create more significant clogging/congestion effects. Incorporating masked/vaccinated individuals or increasing the ventilation rate magnitude reduces the number of total exposed pedestrians. Ventilation direction against pedestrians movement may be beneficial for spreading in scenarios of relatively small number of pedestrians, as a small pocket of clean air created at a small area around the exit may be beneficial. The reverse may, in general, be true, in cases of large crowds occupying a large area at the location of the exit during

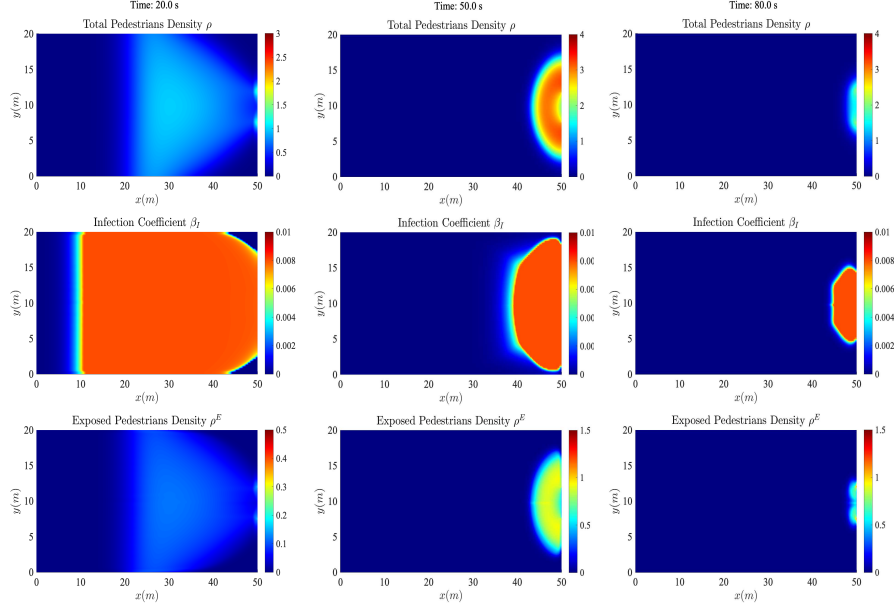


Figure 20: Corridor with a 4 m exit: Total density profiles (top), infection coefficient profile (middle), and exposed pedestrians’ profile at different time instances with  $u_{\max} = 1.4 \text{ m/s}$ ,  $C_0 = 1.2$ , and with no ventilation.

evacuation, as ventilation along the pedestrians flow may result in a larger area of clean air.

## Acknowledgment

Funded by the European Union (ERC, C-NORA, 101088147). Views and opinions expressed are however those of the authors only and do not necessarily reflect those of the European Union or the European Research Council Executive Agency. Neither the European Union nor the granting authority can be held responsible for them.

## References

- [1] J.P. Agnelli, F. Colasuonno, and D. Knopff. A kinetic theory approach to the dynamics of crowd evacuation from bounded domains. *Mathematical Models and Methods in Applied Sciences*, 25(1):109 – 129, 2015.

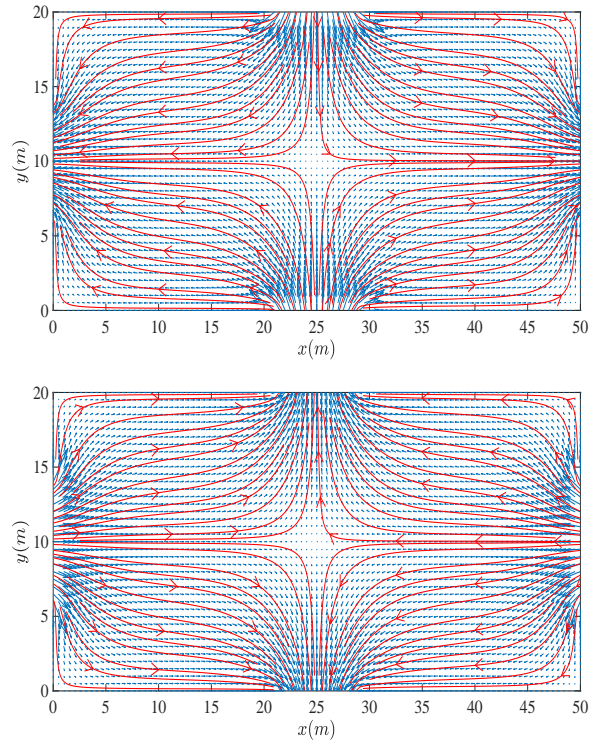


Figure 21: Corridor with a 4 m exit: Velocity field  $\mathbf{U}_G$  vectors (in blue) and the corresponding streamlines (in red), with  $u_{in} = 10$  m/s for pattern I (top) and pattern II (bottom).

- [2] Juan Pablo Agnelli, Bruno Buffa, Damián Knopoff, and Germán Torres. A spatial kinetic model of crowd evacuation dynamics with infectious disease contagion. *Bulletin of Mathematical Biology*, 85(4), 2023.
- [3] R. M. Anderson, H. Heesterbeek, D. Klinkenberg, and T. D. Hollingsworth. How will country-based mitigation measures influence the course of the covid-19 epidemic? *Lancet*, 395:931–934, 2020.
- [4] J. Arino and P. Van den Driessche. A multi-city epidemic model. *Mathematical Population Studies*, 10:175–193, 2003.
- [5] ASHRAE. Ventilation for acceptable indoor air quality, 2015.
- [6] G. Bertaglia and L. Pareschi. Hyperbolic models for the spread of epidemics on networks: Kinetic description and numerical methods. *ESAIM Math. Model. & Numerical Analysis*, 55:381–407, 2021.

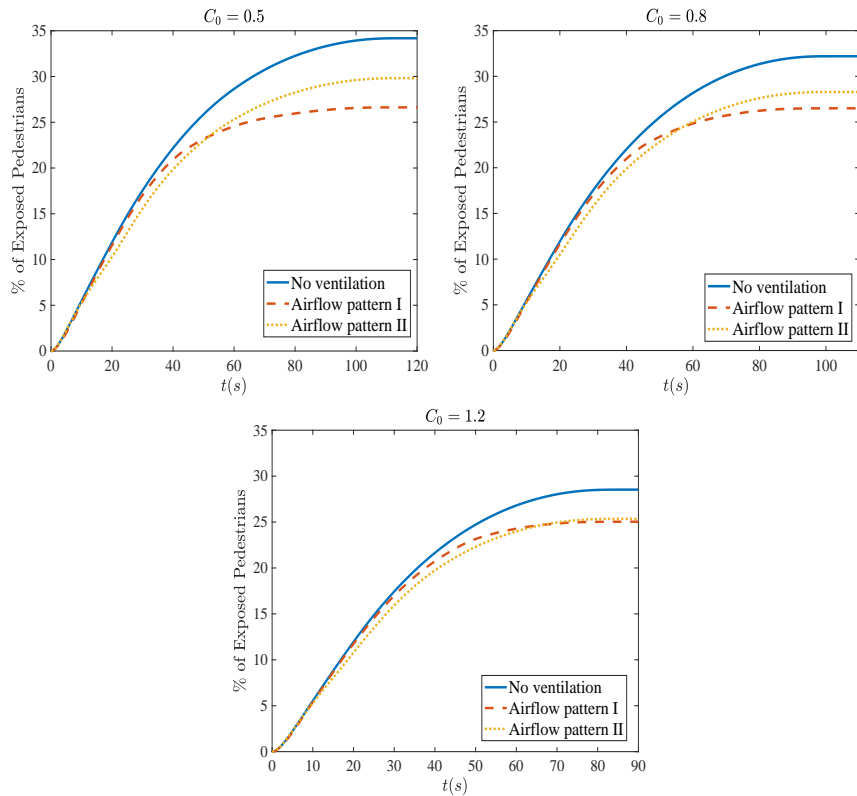


Figure 22: Corridor with a 4 m exit: Percentage of exposed pedestrians with  $u_{\max} = 1.4 \text{ m/s}$  for three different values of  $C_0$ .

- [7] S. Buchmüller and U. Weidmann. Parameters of pedestrians, pedestrian traffic and walking facilities. *IVT Schriftenreihe. Institut für Verkehrsplanung und Transportsysteme (IVT), ETH Zürich*, 132, 2006.
- [8] M. Delmastro and G. Zamariola. Depressive symptoms in response to covid-19 and lockdown: a cross-sectional study on the italian population. *Nature Scientific Reports*, 10, 2020. article no 22457.
- [9] E.F.Toro. *Riemann Solvers and Numerical Methods for Fluid Dynamics*. Springer Berlin, Heidelberg, 2009.
- [10] L. Guan, C. Prieur, L. Zhang, C. Prieur, D. Georges, and P. Bellemain. Transport effect of covid-19 pandemic in france. *Annual Reviews in Control*, 50:394–408, 2020.
- [11] M. Haghani. Crowd dynamics research in the era of covid-19 pandemic: Challenges and opportunities. *Safety Science*, 153, 2022. paper no. 105818.

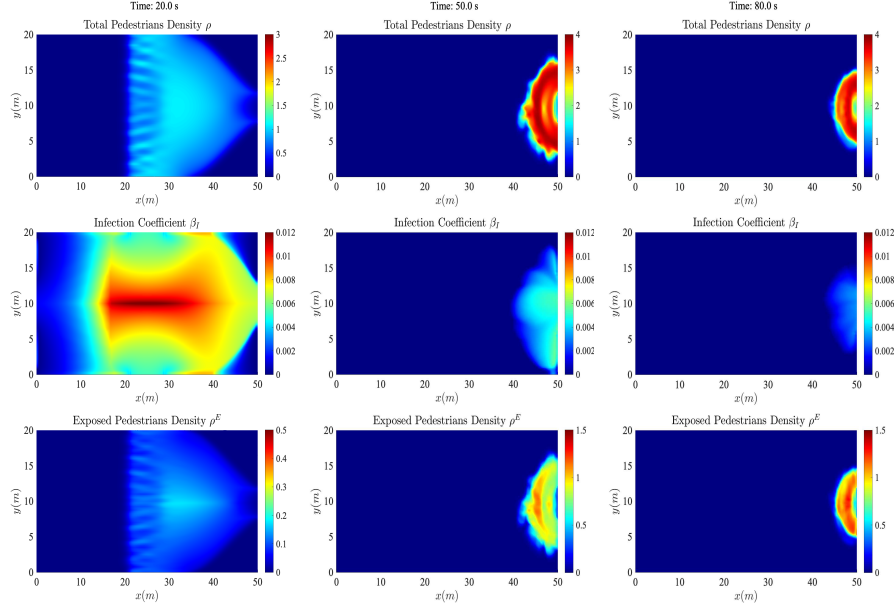


Figure 23: Corridor with a 4 m exit: Total density profiles (top), infection coefficient profile (middle), and exposed pedestrians' profile at different time instances with  $u_{\max} = 1.4 \text{ m/s}$ ,  $C_0 = 0.5$ , and air-flow pattern I.

- [12] F. S. Hanseler and S. Hoogendoorn. Optimal crowd management for congested metro stations. In *In hEART 2018: 7th Symposium of the European Association for Research in Transportation*, 5-7 September, Athens, Greece, 2018.
- [13] A. Harten and J. M. Hyman. Self adjusting grid methods for one-dimensional hyperbolic conservation laws,. *J. Comput. Phys.*, 50:253–269, 1983.
- [14] A.H. Hosseinloo, S. Nabi, A. Hosoi, and M.A. Dahleh. Data-driven control of covid-19 in buildings: a reinforcement-learning approach. *IEEE Trans. on Automation Science and Engineering*, 2023.
- [15] R. L. Hughes. A continuum theory for the flow of pedestrians. *Transp. Res. Part B: Methodological*, 36(6):507, 2002.
- [16] P. Kachroo, S.A. Wadoo, S. J. Al-nasur, and A. Shende. *Pedestrian Dynamics: Feedback Control of Crowd Evacuation*. Springer, Berlin, 2008.
- [17] M. Kaushik. Potential flow theory. In *Theoretical and Experimental Aerodynamics*. Springer, Singapore, 2019.

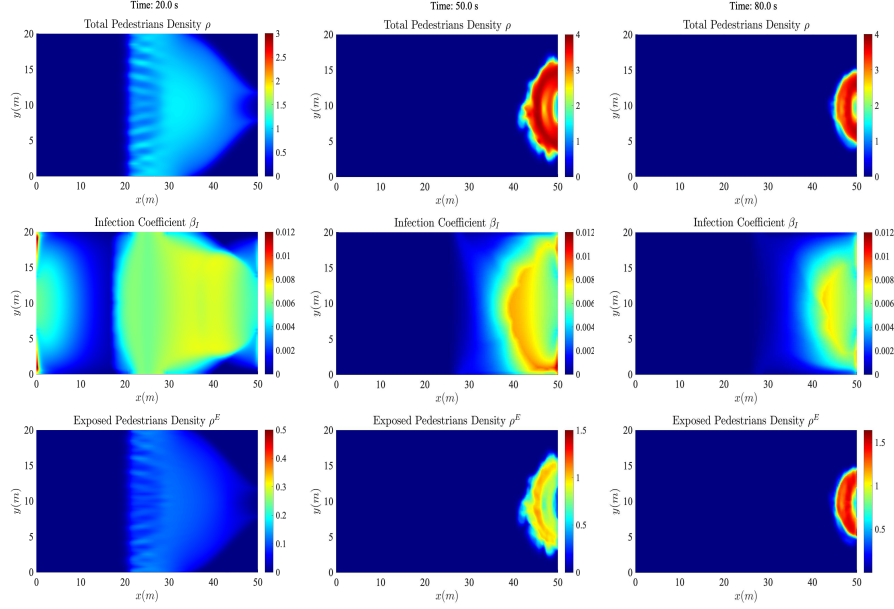


Figure 24: Corridor with a 4  $m$  exit: Total density profiles (top), infection coefficient profile (middle), and exposed pedestrians' profile at different time instances with  $u_{\max} = 1.4 \text{ m/s}$ ,  $C_0 = 0.5$ , and air-flow pattern II.

- [18] D. Kim and A. Quaini. Coupling kinetic theory approaches for pedestrian dynamics and disease contagion in a confined environment. *Math. Models and Meth. in Applied Sciences*, 30:1893–1915, 2020.
- [19] R. J. Leveque. *Finite Volume Methods for Hyperbolic Problems*. Cambridge University Press, U.K., 2002.
- [20] R. J. Leveque. *Finite Difference Methods for Ordinary and Partial Differential Equations: Steady-State and Time-Dependent Problems*. SIAM, Philadelphia, 2007.
- [21] M. J. Lighthill and G.B. Whitham. On kinematic waves, *i*:flow movement in long rivers. *ii*:a theory of traffic on long crowded roads. *Proc. Royal Soc. A*, A229:281–316, 1955.
- [22] Somnath Maity, S. Sundar, and Jörg Kuhnert. A high-resolution meshfree particle method for numerical investigation of second-order macroscopic pedestrian flow models. *Applied Mathematical Modelling*, 131:205 – 232, 2024.

- [23] M.U.B Niazi, C. Canudas-de-Wit, A. Kibangou, and P.-A. Bliman. Optimal control of urban human mobility for epidemic mitigation. In *2021 60th IEEE Conference on Decision and Control (CDC)*, pages 6958–6963, TX, USA, 2021.
- [24] H. J. Payne. Models of freeway traffic and control. *Math. Models Publ. Sys. Simul. Council Proc.*, 28:51–61, 1971.
- [25] H. Qian and X. Zheng. Ventilation control for airborne transmission of human exhaled bio-aerosols in buildings. *Journal of Thoracic Disease*, 10:S2295–S2304, 2018.
- [26] P. S. A. Salam, W. Bock, A. Klar, and S. Tiwari. Disease contagion models coupled to crowd motion and mesh-free simulation. *Math. Models and Meth. in Applied Sciences*, 31:1277–1295, 2021.
- [27] P. S. A. Salam, W. Bock, A. Klar, and S. Tiwari. Coupling pedestrian flow and disease contagion models. In N. Bellomo and L. Gibelli, editors, *Crowd Dynamics, Volume 4: Analytics and Human Factors in Crowd Modeling*, pages 223–246. Springer International Publishing, Cham, 2023.
- [28] L. Sattenspiel and K. Dietz. A structured epidemic model incorporating geographic mobility among regions. *Mathematical Biosciences*, 128:71–91, 1995.
- [29] M. Tizzoni, P. Bajardi, A. Decuyper, G. Kon Kam King, C. M. Schneider, V. Blondel, Z. Smoreda, M. C. Gonzalez, and V. Colizza. On the use of human mobility proxies for modeling epidemics. *Plos Computational Biology*, 10, 2014.
- [30] M. Treiber and A. Kesting. *Traffic flow dynamics: Data, Models and Simulation*. Springer Berlin, Heidelberg, 2013.
- [31] M. Twarogowska, P. Goatin, and R. Duvigneau. Comparative study of macroscopic pedestrian models. *Transportation Research Procedia*, 2:477–485, 2014.
- [32] M. Twarogowska, P. Goatin, and R. Duvigneau. Macroscopic modeling and simulations of room evacuation. *Applied Mathematical Modelling*, 38(24):5781–5795, 2014.
- [33] Arco van Beek, Yan Feng, Dorine C. Duives, and Serge P. Hoogendoorn. Studying the impact of lighting on the pedestrian route choice using virtual reality. *Safety Science*, 174, 2024. Art. no. 106467.
- [34] E. Vynnycky and R. White. *An Introduction to Infectious Disease Modelling*. Oxford Univ. Press, 2010.
- [35] S. A. Wadoo and P. Kachroo. Feedback control of crowd evacuation in one dimension. *IEEE Transactions on Intelligent Transportation Systems*, 11:182–193, 2010.

- [36] L. Willem, F. Verelst, J. Bilcke, N. Hens, and P. Beutels. Lessons from a decade of individual-based models for infectious disease transmission: a systematic review (2006-2015). *BMC Infectious Diseases*, 17, 2017. paper no. 612.
- [37] B. Zhao, Z. Zhang, X. Li, and D. Huang. Comparison of diffusion characteristics of aerosol particles in different ventilated rooms by numerical method. In *ASHRAE Transactions*, volume 110 PART 1, page 88 – 95. 2004.
- [38] H. Zhao. A fast sweeping method for eikonal equations. *Mathematics of Computation*, 74(250):603–627, 2005.

## Appendix

The idea behind the MUSCL scheme is to replace the piecewise constant approximation of the conserved variables of the first-order finite volume scheme by reconstructed states, derived from cell-averaged states. For each computational cell, slope limited, reconstructed left ( $L$ ) and right ( $R$ ) states are obtained and used to calculate the numerical fluxes (namely the Roe and Rusanov ones in this work) at the cell interfaces. Using a piecewise linear approximation of the variables at each cell, results in a scheme that is second-order accurate in space for smooth solutions. This results in the following reconstructed states for each component  $q$  of an unknown vector  $\mathbf{Q}$  along the  $x$ -direction for the  $x_{i+1/2,j}$  interface

$$q_{i+1/2,j}^R = q_{i+1,j} - \frac{\phi(r_{i+1,j}^x)}{4} [(1-\omega)\Delta q_{i+3/2,j} + (1+\omega)\Delta q_{i+1/2,j}], \quad (30)$$

$$q_{i+1/2,j}^L = q_{i,j} + \frac{\phi(r_{i,j}^x)}{4} [(1-\omega)\Delta q_{i-1/2,j} + (1+\omega)\Delta q_{i+1/2,j}], \quad (31)$$

and for the for  $x_{i-1/2,j}$  interface

$$q_{i-1/2,j}^R = q_{i,j} - \frac{\phi(r_{i,j}^x)}{4} [(1-\omega)\Delta q_{i+1/2,j} + (1+\omega)\Delta q_{i-1/2,j}], \quad (32)$$

$$q_{i-1/2,j}^L = q_{i-1,j} + \frac{\phi(r_{i-1,j}^x)}{4} [(1-\omega)\Delta q_{i-3/2,j} + (1+\omega)\Delta q_{i-1/2,j}], \quad (33)$$

where  $\Delta q_{i+1/2,j} = (q_{i+1,j} - q_{i,j})$ ,  $\Delta q_{i-1/2,j} = (q_{i,j} - q_{i-1,j})$ , and

$$r_{i,j}^x = \frac{\Delta q_{i-1/2,j}}{\Delta q_{i+1/2,j}}. \quad (34)$$

The parameter  $\omega$  is allowed to lie in the interval  $[-1,1]$  and for the results presented in this work we have set  $\omega = 0$ . Finally, the function  $\phi(r^x)$  is a limiter function that limits the slope of the piecewise approximations to ensure the solution is Total Variation Diminishing (TVD) thereby avoiding the spurious

oscillations that would otherwise occur around discontinuities or shocks. The limiter is equal to zero when  $r^x \leq 0$  and is equal to unity when  $r^x = 1$ . In this work the van Albada limiter has been utilized, which reads as

$$\phi(r) = \frac{r^2 + r}{1 + r^2}. \quad (35)$$

A similar reconstruction is performed along the  $y$ -direction to obtain the reconstructed values along the  $y_{i,j\pm 1/2}$  interfaces.